Sensors & Actuators: B. Chemical 284 (2019) 305–315

Contents lists available at ScienceDirect

Sensors and Actuators B: Chemical

journal homepage: www.elsevier.com/locate/snb

# Highly selective and sensitive xylene gas sensor fabricated from NiO/$NiCr_2O_4$ p-p nanoparticles

Hongyu Gao, Jie Guo, Yiwen Li, Changlin Xie, Xiao Li, Long Liu, Yi Chen, Peng Sun*, Fangmeng Liu, Xu Yan, Fengmin Liu, Geyu Lu*

*State Key Laboratory of Integrated Optoelectronics, Key Laboratory of Gas Sensors, College of Electronic Science and Engineering, Jilin University, 2699 Qianjin Street, Changchun 130012, Jilin Province, People's Republic of China*

ARTICLE INFO

*Keywords:*
$NiO/NiCr_2O_4$
Xylene detection
Selectivity
Heterojunction
Gas sensor

ABSTRACT

Xylene is a harmful and hazardous volatile organic compound (VOC) indoors, thus selective and sensitive detection for subppm-level xylene is crucial, however a remained challenge. In this work, p-NiO/p-$NiCr_2O_4$ nanocomposites were successfully synthesized through a simple hydrothermal route and used as sensing materials. In the comparative gas sensing test, the sensor fabricated from $NiO/NiCr_2O_4$ (Cr/Ni = 25 at%) nanocomposite exhibited the highest response (66.2–100 ppm) to xylene, which was 37.2 times higher than that of the pure NiO sensor. Moreover, the $NiO/NiCr_2O_4$ nanocomposite gas sensor showed not only superior xylene selectivity with low cross-responses to interfering gases such as ethanol ($S_{xylene}/S_{ethanol}$ = 11.8) and acetone ($S_{xylene}/S_{acetone}$ = 10.2) but also ppb-level detection limit (1.2–50 ppb xylene) at 225 °C. The synergistic catalytic effect between NiO and $NiCr_2O_4$, optimized structural parameters and marked resistive variation due to the formation of nanoscale p-p heterojunctions were regarded as the main reasons for the ultrasensitive and selective xylene detection.

## 1. Introduction

Chemiresistive gas sensors using semiconducting metal oxides have been put into practice for various uses and sensors based on n-type semiconductors prefer to exhibit higher gas responses than p-type oxide semiconductors with same morphologies [1]. However, the n-type oxide semiconductors based sensors are still limited to detect several gases owing to their low selectivity and significant humidity interference [2–4]. P-type oxide semiconductors, as the alternatives, are used to fabricate gas sensors, solving some problems and giving better gas sensing performance at moderate temperatures [5–7]. As we all know, sensitivity and selectivity are chief indicators considered for the gas sensors [8], although good selectivity is always a challenging issue [9,10]. Various strategies have been reported to achieve selective gas sensing [8,11–16], such as optimizing the sensing temperature and loading/doping noble metal catalysts etc. The catalysts include noble metals (Au, Pt, Pd etc.) and some metal compounds (NiO, $Cr_2O_3$, $Co_3O_4$, $NiMoO_4$, $NiWO_4$, $NiCr_2O_4$ etc.), which generally reduce the working temperature of a conductometric sensor for a specific gas and distinguish the target gas from others by the difference in sensitivity [9,11,16–22].

The formation of hetero-nanostructures in the multicompositional sensing materials is also an effective approach to enhance gas selectivity by modulating the conduction near or across the hetero-junctions and synergistic catalytic promotion of a specific sensing reaction [9,19,20,23–25]. In order to make the best use of these benefits, it is essential to form more hetero-interfaces between different sensing materials with small particle sizes through uniform mixing, which can be achieved in the preparation by using a proper physic-chemical route [20]. According to the relevant researches, spinel-type $NiCr_2O_4$ is a p-type semiconductor [21] with general composition formula of $AB_2O_4$, which is synthesized by some methods [26–32], such as hydrothermal pretreatment and thermal treatment. And nickel chromite ($NiCr_2O_4$) is reported to use as magneto-dielectric material [33,34], anode material for lithium ion battery [26,35], catalytic material [22,36] and sensing electrode for gas sensor [37,38] etc. Through literature investigation, the researches on $NiCr_2O_4$ material were relatively less and incomplete till now, and only a few papers reported its applications on gas sensors. Additionally in most of the applications [37–41], the $NiCr_2O_4$ material was used as sensing electrodes for YSZ or NASICON based gas sensors, working at high temperatures and monotonously detecting some gaseous pollutants, especially $NO_x$ etc. And $NiCr_2O_4$ based chemiresistive

* Corresponding authors at: State Key Laboratory of Integrated Optoelectronics, Key Laboratory of Gas Sensors, College of Electronic Science and Engineering, Jilin University, 2699 Qianjin Street, Changchun 130012, Jilin Province, People's Republic of China.
*E-mail addresses:* pengsun@jlu.edu.cn (P. Sun), lugy@jlu.edu.cn (G. Lu).

https://doi.org/10.1016/j.snb.2018.12.152
Received 30 October 2018; Received in revised form 12 December 2018; Accepted 29 December 2018
Available online 30 December 2018

gas sensors were rarely reported for VOC gas detection working at moderate temperatures.

As a representative and ubiquitous pollutant indoors, xylene is commonly used as a solvent in the paint, rubber and leather industries and can be found in the gasoline, cigarette smoke, building and decorating materials etc. Xylene gas is known to cause environmental pollution and some sick symptoms of people. The Center for Disease Control and Prevention published that long-term exposure to 14 ppm xylene and short-term inhalation of as low as 50 ppm xylene can cause throat and eye irritation, fatigue, dizziness, headache and so on [19]. Therefore, it is significant for the effective xylene detection to develop xylene gas sensors with excellent xylene sensing properties. Accordingly in this work, $NiO/NiCr_2O_4$ nanocomposites were obtained and used to fabricate xylene gas sensors. And the $NiO/NiCr_2O_4$ (Cr/Ni = 25 at%) based sensor exhibited superior xylene sensing performance, showing high xylene sensitivity, low ppb-level detection limit and excellent selectivity to xylene gas.

## 2. Experimental

### 2.1. Preparation of the $NiO/NiCr_2O_4$ and $NiCr_2O_4$ samples

All the chemical reagents used in the hydrothermal reaction were analytical grade. First, respectively measure 0.2, 0.5, 1, 1.5, 2 and 4 mmol of $CrCl_3{\cdot}6H_2O$ and added them into their respective beakers with 30 mL of deionized water. Then, successively add 2 mmol of $NiCl_2{\cdot}6H_2O$ and 0.281 g of hexamethylenetetramine (HMT) into the beakers. After 10 min' magnetic stirring, add 2 mL of ethanolamine into the mixed solutions with a pipette gun and keep the solutions stirring for 20 min. Next, the uniformly mixed solutions were respectively transferred to the 45 mL Teflon-lined stainless steel autoclaves, which were then sealed and put into a hot oven with a constant temperature of 180 °C for 8 h. When the stainless steel reactors cooled to room temperature, centrifuge the resulting precipitates for five times with ethanol and deionized water alternatively, then dry the products at 80 °C overnight in an oven. The final $NiO/NiCr_2O_4$ nanocomposites with Cr/Ni ratios of 10, 25, 50, 75 and 100 at% were obtained after heat treatment at 500 °C for 3 h in a muffle furnace. While the pure $NiCr_2O_4$ (Cr/Ni = 200 at%) sample was prepared after sintering for 2 h at 1000 °C.

### 2.2. Preparation of the NiO and $Cr_2O_3$ samples

In our experiment, pure NiO and $Cr_2O_3$ samples, as contrastive materials, were also synthesized by the similar hydrothermal routes. In brief, singly measure 0.475 g of $NiCl_2{\cdot}6H_2O$ and 0.133 g $CrCl_3{\cdot}6H_2O$ and add them separately into two beakers with 30 mL of deionized water respectively. And the subsequent treatments to the solutions were the same as those in the $NiO/NiCr_2O_4$ preparation above.

### 2.3. Characterization

The morphologies of the obtained materials were characterized using field emission scanning electron microscopy (FESEM, JSM-7500 F JEOL) and transmission electron microscopy (TEM, JEM-2200FS JEOL). And the analyses of energy dispersive X-ray spectroscopic (EDS) were obtained from TEM attachment. The crystallinities and phases of the samples were collected from X-ray diffraction analysis (XRD, Rigaku D/Max-2550) with Cu Kα radiation (λ = 1.541 Å; 40 kV, 350 mA). The composition analyses were obtained from X-ray photoelectron spectrograph (XPS) with Mg-Kα X-ray (1253.6 eV Specs XR50). The pore size distributions and surface areas were measured using the Brunauer-Emmett-Teller method (BET, Micromeritics Gemini VII apparatus) with $N_2$ adsorption-desorption.

### 2.4. Fabrication and measurement of gas sensor

The chemiresistive gas sensor is mainly composed of four parts: 1. A 4 mm long ceramic tube (internal diameter: 0.8 mm, external diameter: 1.2 mm), where a pair of gold electrodes with four Pt wires have been installed originally. 2. Sensing material layer (thickness: ~42 μm) on the surface of ceramic tube. Taking the $NiO/NiCr_2O_4$ (Cr/Ni = 25 at%) based sensor as an example here. Mix the obtained powder with deionized water to form a slurry and coat the slurry uniformly on the whole surface of the ceramic tube. Then put the well-coated tube in the muffle furnace heating at 500 °C for 3 h in air. 3. A Ni-Cr alloy coil heater, it was inserted through the well-coated and sintered ceramic tube, controlling the working temperature via the flowing current. 4. A hexagon base, which supported the well-coated and sintered ceramic tube through welding. After ageing, the as-prepared sensors were tested through the static test system at a laboratory conditions (20 °C, 10% RH). The detailed descriptions about the sensor architecture and sensing-test system were shown in our previous works [42,43]. The changing resistances were collected as sensor signals and the ratio ($R_g/R_a$) between resistances in target gas ($R_g$) and fresh air ($R_a$) is defined as gas response for the p-type gas sensor. Moreover, the times needed for the sensor resistance to achieve 90% of the total saturation changes were defined as the response and recovery times after the sensor was put in the target gases and fresh air, respectively.

## 3. Results and discussion

### 3.1. Structural and morphological characteristics

XRD patterns of the prepared $NiO/NiCr_2O_4$ nanostructures with different Cr/Ni ratios of 10–100 at% and the pure $NiCr_2O_4$ (Cr/Ni = 200 at%) are shown in Fig. S1. Obviously in Fig. S1a, two phases of NiO and $NiCr_2O_4$ were observed in all the $NiO/NiCr_2O_4$ nanostructures and the $NiCr_2O_4$ peaks were enhanced while NiO peaks weakened with the increasing Cr/Ni ratios (10–100 at%). And a single phase of $NiCr_2O_4$ was found in Fig. S1b, indicating the formation of pure $NiCr_2O_4$. Besides, the XRD patterns of NiO, $Cr_2O_3$ and $NiO/NiCr_2O_4$ (Cr/Ni = 25 at%) are shown in Fig. 1. The NiO and $Cr_2O_3$ samples matched well with the standard NiO (Fm-3 m, JCPDS No. 73-1519) and $Cr_2O_3$ (R-3c, JCPDS No. 82-1484) patterns respectively, and no other-phase peaks were detected. And the sharp and intensive diffraction peaks of the pure NiO sample indicated its large crystallite size and high crystalline quality [44]. As for the $NiO/NiCr_2O_4$ (Cr/Ni = 25 at%) XRD pattern shown in Fig. 1b, besides the five obvious NiO characteristic peaks, other characteristic peaks of another phase were also observed, which were indexed to the (220), (311), (422) and (511) crystal planes of $NiCr_2O_4$ (Fd-3 m, JCPDS No. 75-1728) respectively. Thus the as-obtained $NiO/NiCr_2O_4$ materials were proved to be composited by NiO and $NiCr_2O_4$ phases through the XRD analyses.

To further confirm the compositions of the obtained materials, XPS analyses of all the samples are shown in Fig. 2. Clearly in the XPS survey spectrum (Fig. 2a and d), the signals of Ni, Cr and O elements were observed in the $NiO/NiCr_2O_4$ nanostructures with Cr/Ni ratios of 10–100 at% and the pure $NiCr_2O_4$ sample, no signal of Cr was found in the NiO and no signal of Ni was found in the $Cr_2O_3$ sample as well. In the Fig. 2b and e of Ni 2p spectra, the peaks located around 855.3 and 873.2 eV were assigned to Ni $2p_{3/2}$ and Ni $2p_{1/2}$ of $Ni^{2+}$ [22,26]. Additionally from the Cr 2p spectra shown in Fig. 2c and f, Cr $2p_{3/2}$ and Cr $2p_{1/2}$ of $Cr^{3+}$ peaked near 576.5 and 586.2 eV, respectively [22,26]. Accordingly, the XPS results further confirmed the existence of NiO, $Cr_2O_3$ and $NiCr_2O_4$ phases, indicating the formation of the pure samples and $NiO/NiCr_2O_4$ composites in this work.

The morphologies of the as-prepared pure $Cr_2O_3$, NiO, $NiCr_2O_4$ and $NiO/NiCr_2O_4$ (Cr/Ni = 10–100 at%) samples are shown in Fig. 3. Obviously, from the high-resolution SEM images of $Cr_2O_3$ (Fig. 3a) and NiO (Fig. 3b) samples, both of $Cr_2O_3$ and NiO nanostructures were

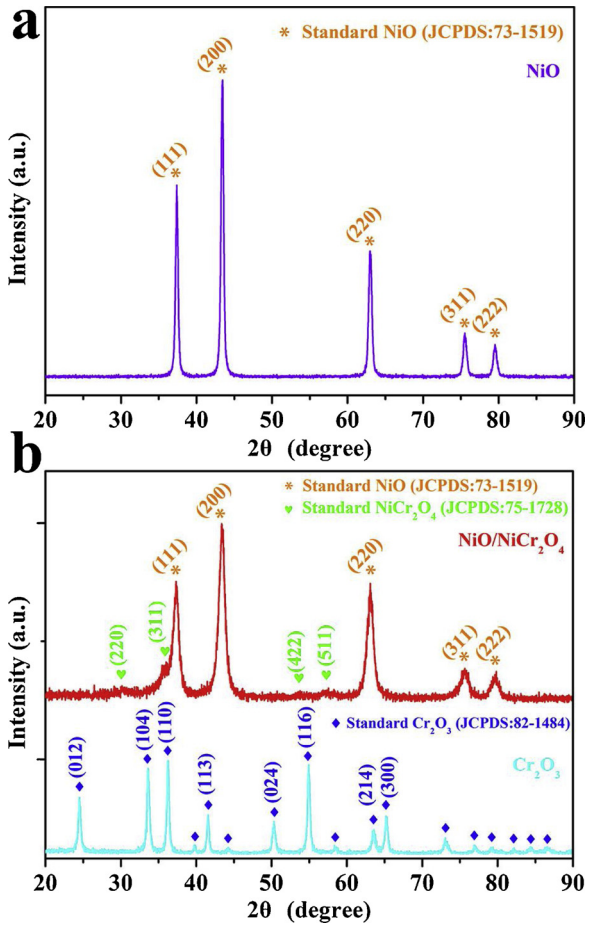


**Fig. 1.** XRD patterns of the obtained **(a)** NiO, **(b)** $Cr_2O_3$ and NiO/$NiCr_2O_4$ (Cr/Ni = 25 at%) nanostructures.

assembled from many nanoparticles with uniform particle sizes (~40 nm). Fig. 3c-g show the high resolution morphologies of the NiO/$NiCr_2O_4$ nanocomposites with Cr/Ni ratios of 10, 25, 50, 75 and 100 at %, respectively. It could be found that all the NiO/$NiCr_2O_4$ samples showed irregular nanostructures, which were assembled from many small NiO and $NiCr_2O_4$ nanoparticles. Besides, similar characterization result could be obtained from the SEM image of the pure $NiCr_2O_4$ sample (Fig. 3h) that it was also assembled from many $NiCr_2O_4$ nanoparticles.

TEM characterization was also applied for further investigation. Fig. 4a-c are the TEM images with different resolutions of the pure NiO sample. Obviously the NiO nanostructure was assembled from many nanoparticles with uniform particle sizes (~40 nm), which showed a same morphology in the SEM image (Fig. 3b). And from the high-resolution TEM (HRTEM) image shown in Fig. 4c, clear lattice fringes with a spacing of 0.244 nm were observed on a NiO nanoparticle, corresponding to the (111) lattice plane of NiO nanostructure. From the STEM and elemental distribution images of NiO in Fig. 4d-f, both O and Ni elements were detected and their distributions were nearly the same, indicating the formation of uniform NiO nanoparticles. The similar discussions were also applied to the NiO/$NiCr_2O_4$ (Cr/Ni = 25 at%) sample and typical TEM and HRTEM images of this NiO/$NiCr_2O_4$ nanocomposite are shown in Fig. 4g-i. Many small nanoparticles were found in Fig. 4g, and the particle sizes of these uniform nanoparticles were measured about 8 nm in Fig. 4h. Moreover, two kinds of lattice fringes with spacing of 0.213 (marked orange) and 0.256 nm (marked green) were found clearly in Fig. 4i, which were attributed to the NiO (200) and $NiCr_2O_4$ (311) lattice planes, respectively. And these findings are consistent with the XRD results presented in Fig. 1b. The nanocomposite was also investigated by STEM (Fig. 4j) and elemental mapping (Fig. 4k-m). All the three elements (O, Ni and Cr) were detected and uniformly distributed over the nanoparticles. It could be also found that the signal of Cr element was weaker than that of O and Ni, indicating that the content of Cr was relatively less. And all the results obtained from TEM analyses above further indicated that the NiO/$NiCr_2O_4$ nanocomposite was uniformly assembled from many small NiO and $NiCr_2O_4$ nanoparticles.

### 3.2. Gas sensing characteristics

Comprehensive gas-sensing tests of our obtained materials were carried out and shown in this section. First, comparative tests among the six sensors based on the NiO/$NiCr_2O_4$ nanostructures with different Cr/Ni ratios of 10–100 at% and the pure $NiCr_2O_4$ (Cr/Ni = 200 at%) were performed and the results are shown in Fig. 5. Compared with

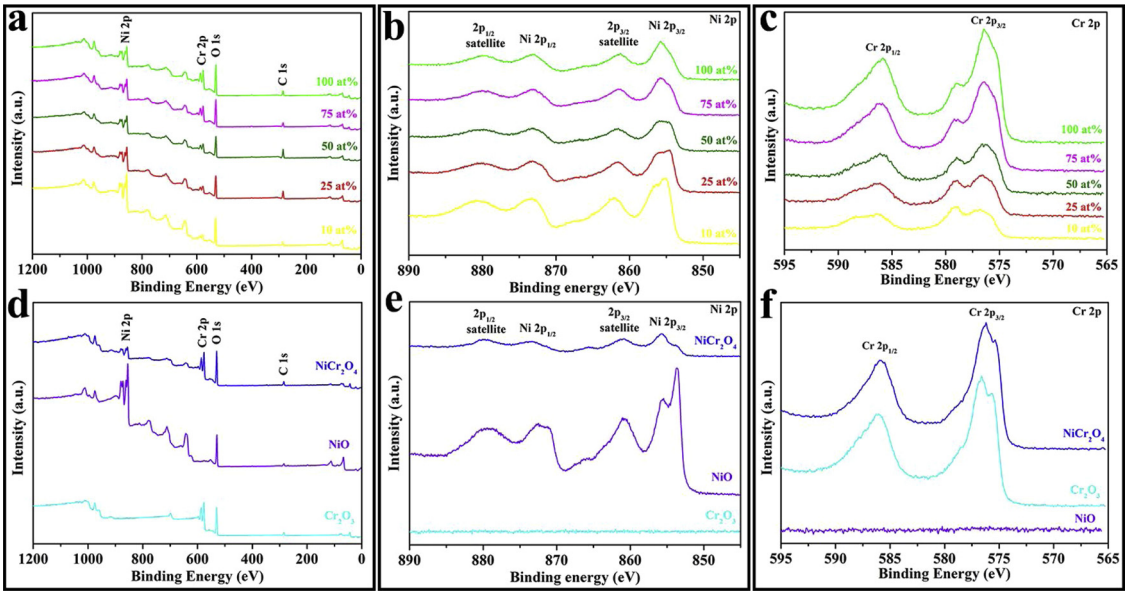


**Fig. 2. (a, d)** XPS survey scan, **(b, e)** Ni 2p and **(c, f)** Cr 2p XPS spectra of all the obtained NiO/$NiCr_2O_4$ nanostructures with different Cr/Ni ratios of 10–100 at% and the pure samples, respectively.

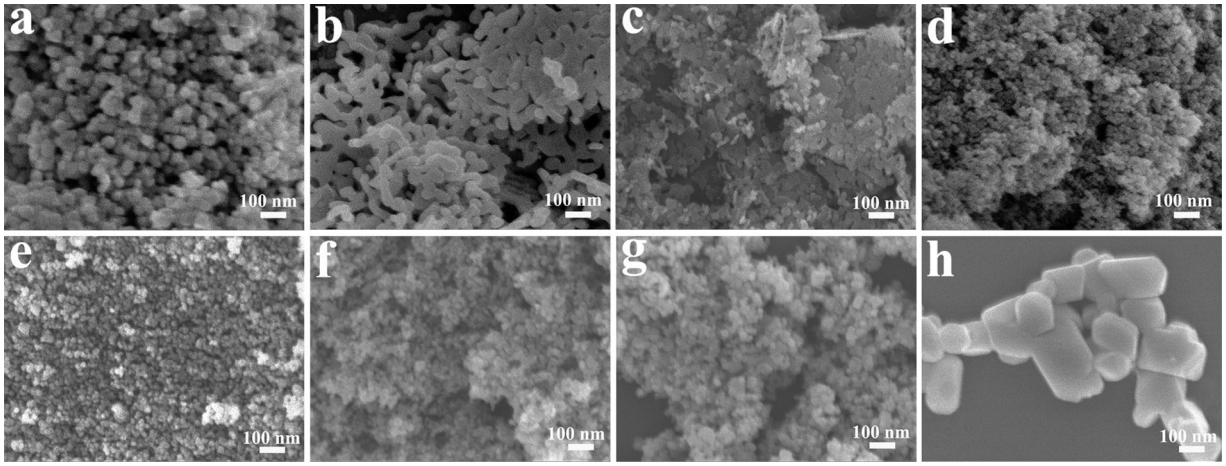


**Fig. 3.** SEM images of the obtained **(a)** $Cr_2O_3$, **(b)** NiO and NiO/$NiCr_2O_4$ nanostructures with different Cr/Ni ratios of **(c)** 10 at%, **(d)** 25 at%, **(e)** 50 at%, **(f)** 75 at%, **(g)** 100 at% and **(h)** pure $NiCr_2O_4$ (Cr/Ni = 200 at%) nanostructure, respectively.

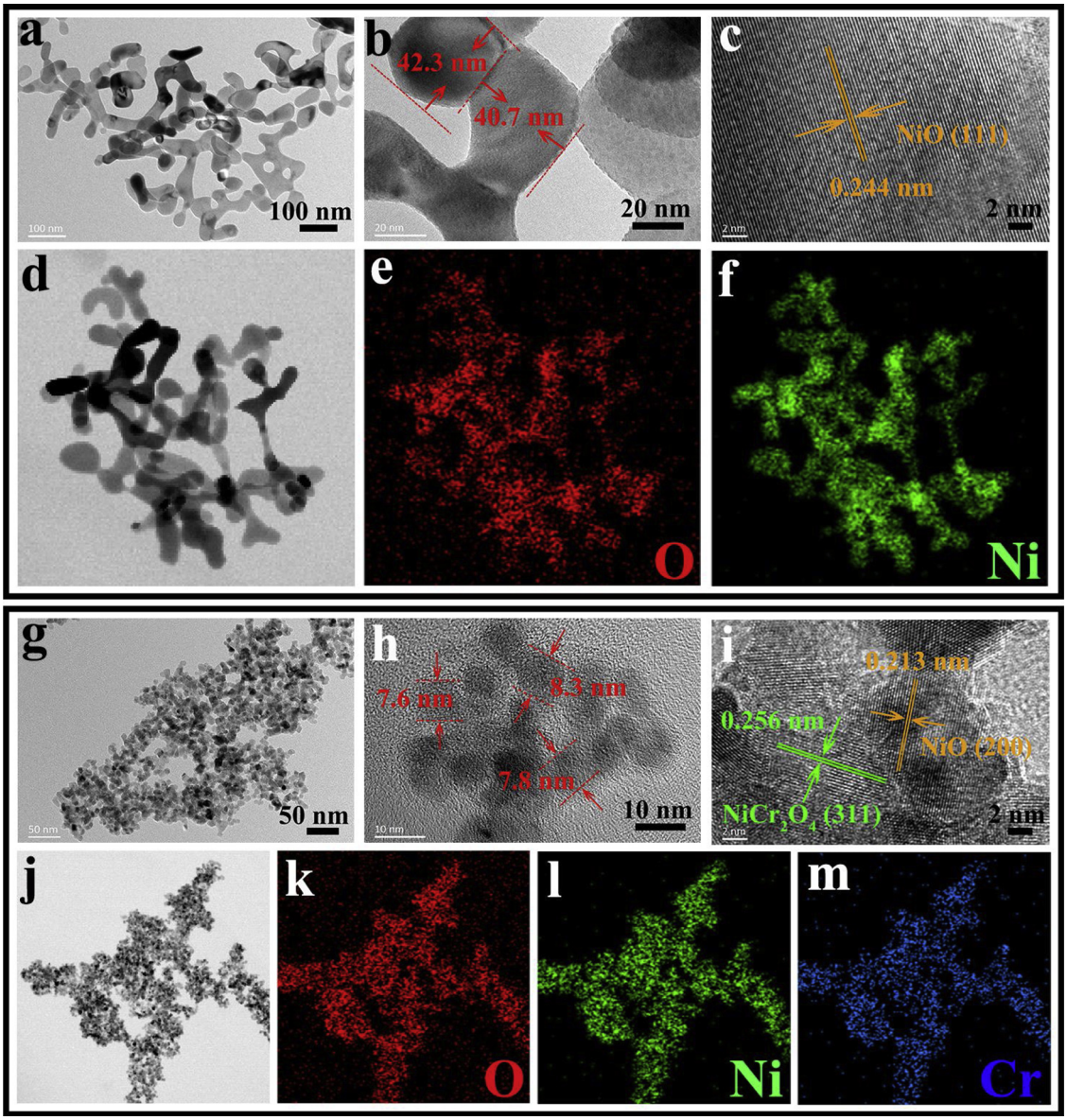


**Fig. 4.** TEM and elemental mapping images of prepared **(a–f)** NiO and **(g–m)** NiO/$NiCr_2O_4$ (Cr/Ni = 25 at%) samples.

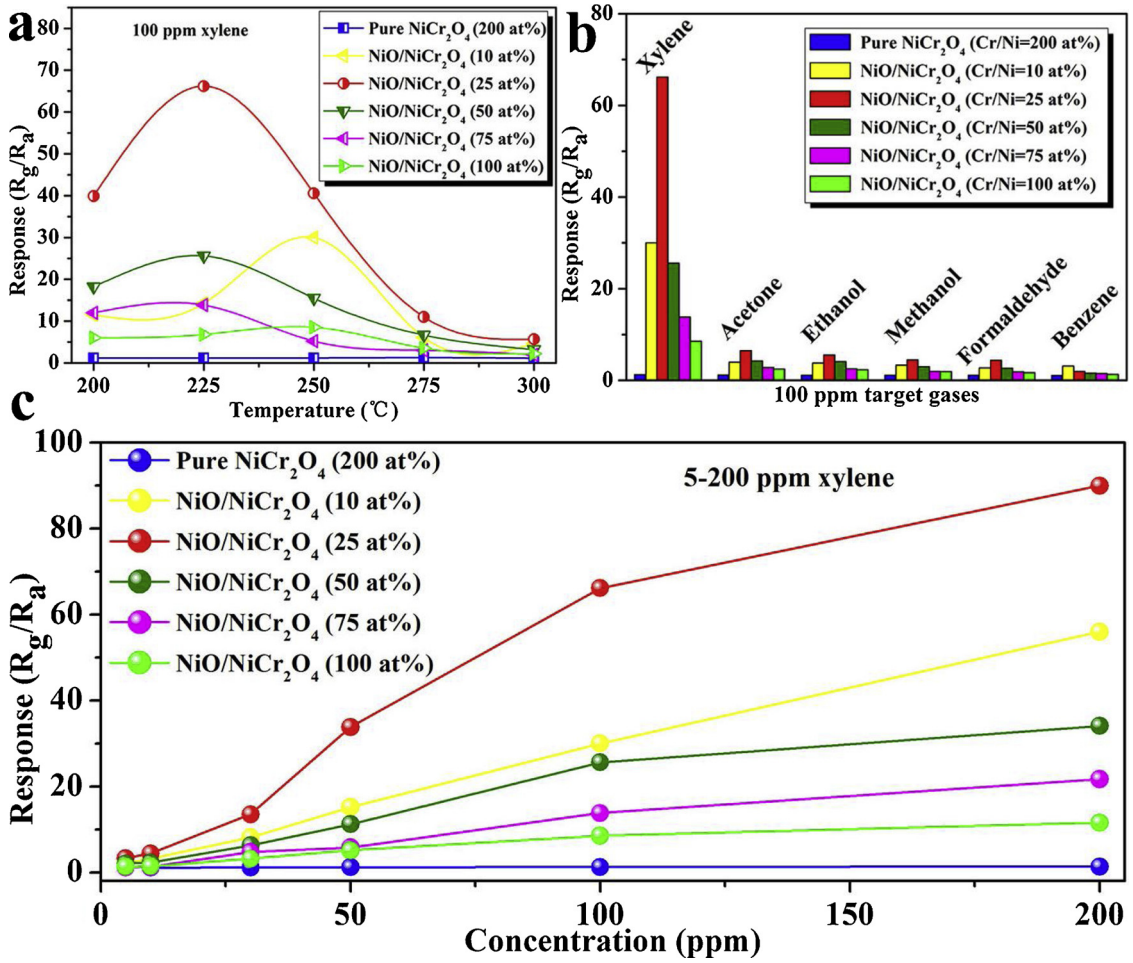


**Fig. 5. (a–c)** Response-temperature, response-target gas and response-concentration properties of the six sensors based on the $NiO/NiCr_2O_4$ nanostructures with different Cr/Ni ratios of 10–100 at% and the pure $NiCr_2O_4$ (Cr/Ni = 200 at%).

other five sensors in Fig. 5a, the sensor based on the $NiO/NiCr_2O_4$ sample with a Cr/Ni ratio of 25 at% exhibited much higher sensitivities to 100 ppm xylene at 200–300 °C and showed the highest xylene sensitivity (66.2) at 225 °C. Fig. 5b shows the selectivity of the sensors among six VOC gases. Obviously, the $NiO/NiCr_2O_4$ (Cr/Ni = 25 at%) based sensor showed superior xylene selectivity against other interfering gases. Response-concentration properties of all the six sensors are depicted in Fig. 5c. Clearly the xylene response of the $NiO/NiCr_2O_4$ (Cr/Ni = 25 at%) based sensor fiercely increased with the increasing xylene concentration. And to a same concentration of xylene, the $NiO/NiCr_2O_4$ (Cr/Ni = 25 at%) based sensor showed the highest response among all the six gas sensors. According to the results above, the sensor based on the $NiO/NiCr_2O_4$ sample with a Cr/Ni ratio of 25 at% exhibited the best xylene sensing performance among all the sensors based on materials with different Cr/Ni ratios. Therefore the following sensing tests and discussions were mainly concentrated on the $NiO/NiCr_2O_4$ nanostructure with a Cr/Ni ratio of 25 at%.

As shown in Fig. 6a, responses to 100 ppm xylene of NiO, $NiO/NiCr_2O_4$ (Cr/Ni = 25 at%) and $Cr_2O_3$ based gas sensors increased first and then decreased with temperature increasing, showing relatively lower optimal operating temperatures (225 °C) for the three sensors. Obviously, the $NiO/NiCr_2O_4$ (Cr/Ni = 25 at%) based gas sensor showed much higher gas responses to 100 ppm xylene than those of the pure NiO and $Cr_2O_3$ sensors at 175–275 °C, for example, exhibiting a 37.2 times higher xylene response of 66.2 at 225 °C compared with the unmodified NiO sensor. And at their optimal operating temperatures (225 °C), selectivity among six VOC gases (xylene, acetone, ethanol, methanol, formaldehyde and benzene) was tested in Fig. 6b. It was clear that the sensor based on $NiO/NiCr_2O_4$ (Cr/Ni = 25 at%) nanocomposite displayed a much higher response and better selectivity to xylene than to other target gases. In contrast, the sensor based on pure NiO exhibited negligibly low responses to all six analyte gases (1.03–1.78), nearly no selectivity at all. As selectivity is a chief indicator of gas sensor for its practical application [8], further research results on selectivity are shown in Fig. 6c and d. Gas responses of the $NiO/NiCr_2O_4$ (Cr/Ni = 25 at%) gas sensor to six VOC gases at different operating temperatures are depicted in Fig. 6c, showing a reliable xylene selectivity among interfering gases in a wide temperature range centered at 225 °C. Moreover, the cross-selectivity of the sensor to other VOCs gases was also analyzed and shown in Fig. 6d. The response ratios of xylene to ethanol ($S_{xylene}/S_{ethanol}$) and acetone ($S_{xylene}/S_{acetone}$) were calculated and plotted as the function of the working temperature. Significantly, the $NiO/NiCr_2O_4$ (Cr/Ni = 25 at%) gas sensor showed superior xylene selectivity against other interfering gases, giving high response ratios to ethanol ($S_{xylene}/S_{ethanol}$ = 11.8) and acetone ($S_{xylene}/S_{acetone}$ = 10.2) at 225 °C. Fig. 6e shows the response curves of the three sensors to various concentrations of xylene and compared with the sensors based on pure materials, the $NiO/NiCr_2O_4$ (Cr/Ni = 25 at%) nanocomposite based gas sensor exhibited rapidly increased gas responses even at the lower xylene concentrations. And the $NiO/NiCr_2O_4$ (Cr/Ni = 25 at%) based gas sensor gave a response of 1.2–50 ppb xylene (Fig. 6f), indicating its low subppm-level detection limit. Accordingly, the $NiO/NiCr_2O_4$ (Cr/Ni = 25 at%) based gas sensor showed superior xylene cross-selectivity, high gas response and low detection limit, indicating its potential application for selective and sensitive xylene detection.

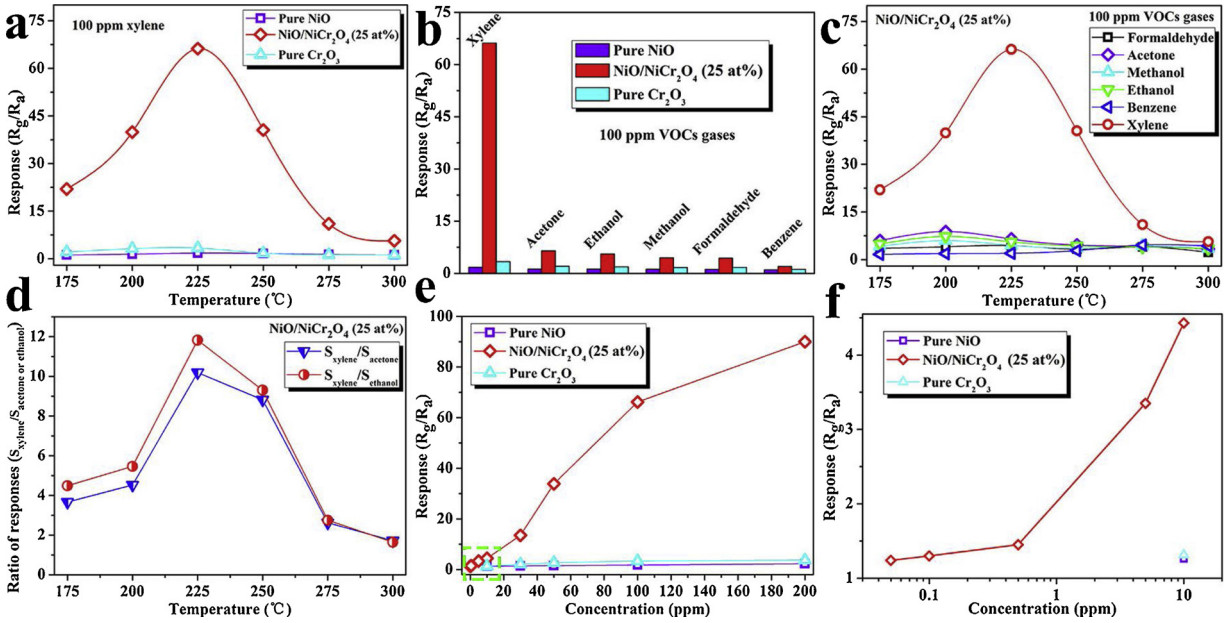


**Fig. 6. (a, b)** Response-temperature curves and selectivity of the three sensors based on the NiO, $NiO/NiCr_2O_4$ (Cr/Ni = 25 at%) and $Cr_2O_3$ samples. **(c, d)** Selectivity properties of the $NiO/NiCr_2O_4$ (Cr/Ni = 25 at%) sensor vs working temperatures. **(e, f)** Response curves of the three sensors to different concentrations of xylene.

Furthermore, the dynamic response-recovery transients of the sensors are displayed in Fig. 7. It was apparent that all the resistance curves stepwise increased with the increasing xylene concentrations (Fig. 7a-c). And the $NiO/NiCr_2O_4$ (Cr/Ni = 25 at%) gas sensor showed good response-recovery performance even in the subppm-level xylene gas (Fig. 7d), giving a low detection limit (50 ppb). Additionally in Fig. 7e, the response and recovery times were tested in 100 ppm xylene gas and measured to be 1217 and 591 s respectively. The response-recovery times were relatively longer, because long time was needed for the $NiO/NiCr_2O_4$ sensor to reach saturation, which resulted from the low reactivity of methyl benzenes [7,17] and the nanoparticle-aggregated configuration [45]. However, it could be found that the $NiO/NiCr_2O_4$ sensor showed a faster speed to xylene at the first several minutes upon exposure to xylene gas, even though it did not reach the saturated gas response (˜66.2). And in the practical detection, ultrahigh or saturated gas response was generally not the necessary requirement, thus the $NiO/NiCr_2O_4$ sensor could exhibit relatively faster response speed actually. For example, after exposure to 100 ppm xylene for 3 min (the green point in Fig. 7e), the $NiO/NiCr_2O_4$ sensor showed a relatively higher response of 16.9 with a shorter 90% response time of 156 s, both of which were satisfactory and acceptable indicators for practical xylene detection. Additionally, the $NiO/NiCr_2O_4$ (Cr/Ni = 25 at%) gas sensor was tested continuously in the laboratory condition for 30 days, the collected resistance and response values were plotted in Fig. 7f. Obviously, the initial resistances at 225 °C and xylene (100 ppm) responses varied in small ranges around respectively 2.6 MΩ and 64.2 during the tested 30 days. These results demonstrated that the $NiO/NiCr_2O_4$ based xylene sensor had good long-term stability, which might result from the stable configuration assembled uniformly by fine nanoparticles as well as the thermally stable spinel-type $NiCr_2O_4$ structure [21,36,46].

Water vapor interference was considered here, as the resistance curve of the $NiO/NiCr_2O_4$ (Cr/Ni = 25 at%) gas sensor to 100 ppm of xylene at 10% RH, 225 °C was discussed before in Fig. 7e, thus only three transient curves at 30, 60 and 90% RH are shown in Fig. 8a. Their response and resistance values were marked out (Fig. 8a) and their relation curves are shown in Fig. 8b and c, respectively. Clearly, the resistance increased and response decreased with the increasing RH, which could be explained by the competition for pre-adsorbed oxygen species between target gas and water vapor [1]. Although water vapors had some negative effects on the gas sensing performance, the $NiO/NiCr_2O_4$ (Cr/Ni = 25 at%) gas sensor still showed higher gas responses, even a relatively higher response (43.6–100 ppm xylene) at high 90% RH, which was acceptable for real applications.

Here, a comparison among the xylene gas sensors based on various materials [9,10,19,20,47–54] was made and shown in Table 1. It could be concluded that our $NiO/NiCr_2O_4$ (Cr/Ni = 25 at%) gas sensor in this work showed superior xylene sensing properties than most of the reported xylene sensors, exhibiting lower working temperature, higher gas response, low detection limit and excellent selectivity etc. Interestingly, the sensing materials used in most of the reported xylene gas sensors consist of one or two catalytic materials, such as catalytic metals (Au, Ag, Pd etc.) and some metal compounds (NiO, $Cr_2O_3$, $Co_3O_4$, $NiMoO_4$, $NiWO_4$, $NiCr_2O_4$ etc.). Moreover, owing to the synergistic catalytic promotion, the sensing materials compounded of two catalysts prefer to exhibit excellent xylene sensing performance, especially superior selectivity, such as reported $NiO/NiMoO_4$, $NiO/NiWO_4$, $Cr_2O_3/ZnCr_2O_4$ materials [9,19,20] and the $NiO/NiCr_2O_4$ composite in this work. So catalytic promotion may be a considerable factor for xylene detection, which has positive effect on xylene-sensing performance, although more detailed and systematic studies are necessary to confirm this.

### 3.3. Gas sensing mechanism

As we all know, the enhanced sensing performance always resulted from the co-effect of multi-factors [5,8,55], thus in this section, the mechanism for the ultrasensitive and highly selective xylene sensing performance was discussed in detail from multiple aspects. The particle size was first considered here, because a move to smaller particles can significantly increase the sensitivity of a sensor on the basis of the experimental and theoretical evidence, especially when the particle sizes were comparable to or smaller than twice the hole accumulation layer thickness ($t_{HAL}$) [5,20,55]. As shown in TEM images, the particles of the $NiO/NiCr_2O_4$ (Cr/Ni = 25 at%) composite and pure NiO sensing materials were measured to be ˜8 and ˜40 nm, respectively. Clearly the average particle size of $NiO/NiCr_2O_4$ composite (˜8 nm) was comparable to $2t_{HAL}$ and significantly smaller than that of NiO particles (˜40 nm), which could effectively promote the variation of resistance, thus exhibiting high sensitivity. Moreover, the uniform particle size

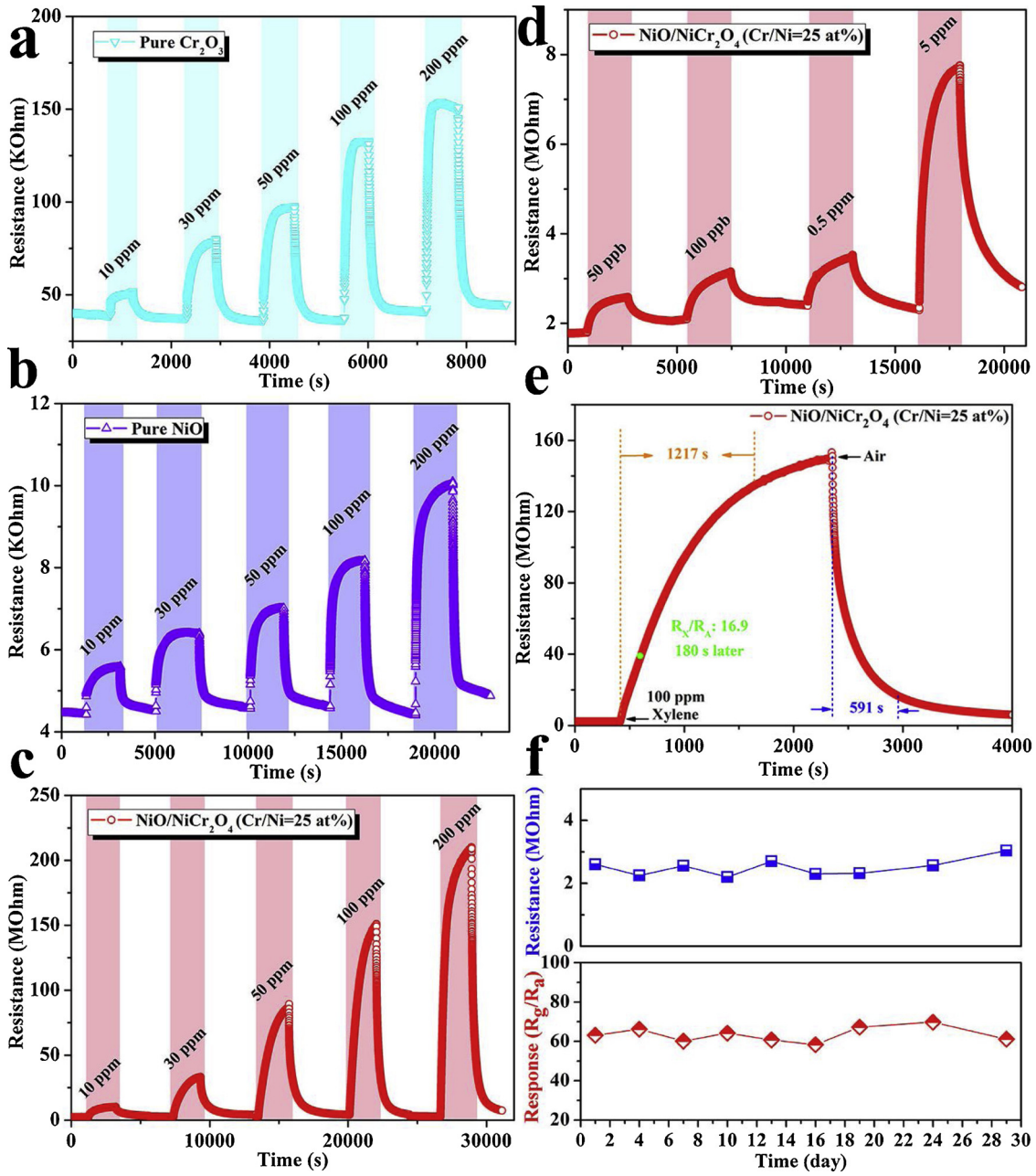


**Fig. 7.** Dynamic resistances of the **(a)** $Cr_2O_3$, **(b)** NiO and **(c, d)** NiO/$NiCr_2O_4$ (Cr/Ni = 25 at%) sensors at different concentrations of xylene. **(e)** Response-recovery times of the NiO/$NiCr_2O_4$ (Cr/Ni = 25 at%) sensor to 100 ppm of xylene **(f)** Initial resistances in fresh air and responses to 100 ppm xylene of the NiO/$NiCr_2O_4$ (Cr/Ni = 25 at%) sensor as a function of test days.

(~8 nm) of NiO/$NiCr_2O_4$ (Cr/Ni = 25 at%) composite was exactly in the reported diameter range (1–10 nm), where the maximum of sensitivity appeared [55].

Furthermore, gas-accessible mesoporous structure with large surface area also has positive effect on the sensing properties [9]. $N_2$ adsorption-desorption curves and pore size distributions of the NiO and NiO/$NiCr_2O_4$ (Cr/Ni = 25 at%) materials are shown in Fig. 9, similar characterization results of obtained samples with other Cr/Ni ratios are depicted in Fig. S2. As shown in Fig. 9e and f, abundant mesopores with a peak pore size of 23.87 nm and high specific surface area (99.8 $m^2 g^{-1}$) were founded in the NiO/$NiCr_2O_4$ (Cr/Ni = 25 at%) composite, which were much higher than those (2.57 nm and 23.7 $m^2 g^{-1}$) of the pure NiO sample (Fig. 9b and c). According to the textural parameters summarized in Table 2, the average pore volume of the NiO/$NiCr_2O_4$ (0.57 $cm^3 g^{-1}$) with Cr/Ni = 25 at% was also much higher than that of the pure NiO (0.06 $cm^3 g^{-1}$). Based on these BET results above, the NiO/$NiCr_2O_4$ composite showed a mesoporous structure with much larger surface area, pore size and pore volume compared with those of the NiO sample. Accordingly, this kind of structure could provide sufficient adsorption sites on the surface of NiO/$NiCr_2O_4$ material and facilitated gas transfer, which was crucial for the interactions between sensing material and target gas, thus promoting the gas response [9,19,45].

The formation of $NiCr_2O_4$ or the composite between NiO and $NiCr_2O_4$ also plays important effects on promoting the gas response. NiO material is known to perform p-type semiconductivity [19] and $NiCr_2O_4$ is also a p-type semiconductor [21]. Thus more nanoscale p-p heterojunctions existed across the interfaces of the small NiO and $NiCr_2O_4$ nanoparticles in the intimately and uniformly mixed NiO/$NiCr_2O_4$ composite (seen in TEM analyses). Actually the p-p

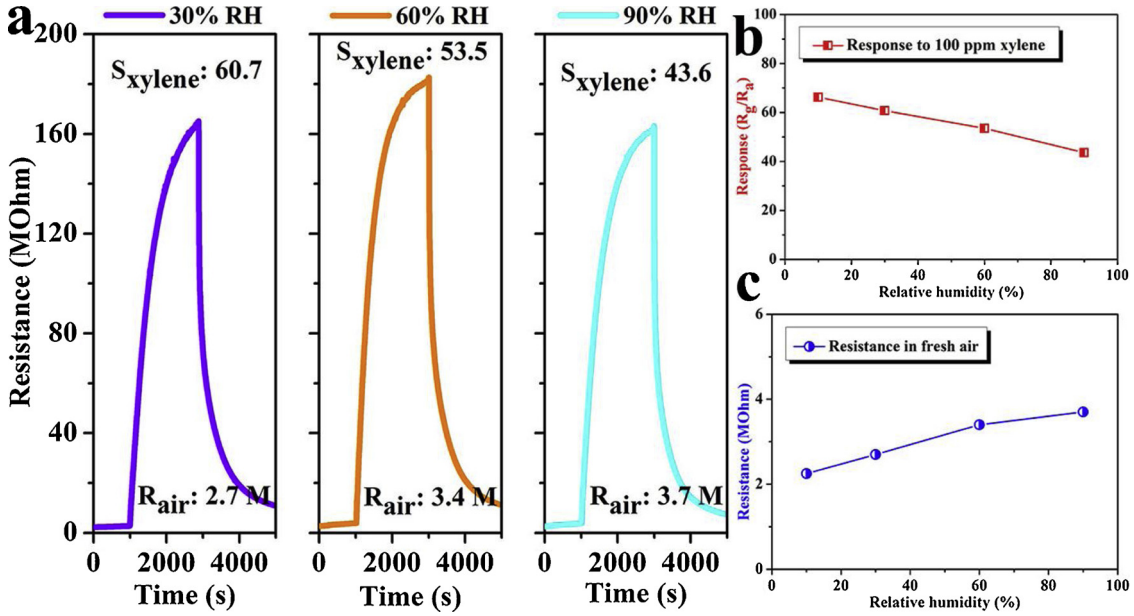


**Fig. 8. (a)** Dynamic response curves of the NiO/$NiCr_2O_4$ (Cr/Ni = 25 at%) sensor to 100 ppm xylene at various humidity and their corresponding **(b)** response and **(c)** resistance relations.

heterojunctions across the interfaces could be regarded as adjustable resistors with high resistances, because the potential barrier heights would shift owing to the charge transfers and showed different resistances in different gases and temperatures. As for the resistive gas sensors at micro level, conduction was accomplished through charge carrier's transfer among the connected grains [56], exhibiting resistance simultaneously. According to the theoretical and experimental evidences in reported literatures and this work [21,32,57–59], the band gaps of NiO and $NiCr_2O_4$ were respectively about 3.4 and 1.7 eV and the pure NiO showed higher conductivity at high temperatures, its resistance at 225 °C (~4.3 KΩ) was much lower than that of $NiCr_2O_4$ material (~2.7 MΩ) as well as the resistances of p-p heterojunctions between NiO and $NiCr_2O_4$ nanoparticles. Thus in this configuration of NiO/$NiCr_2O_4$ composite, where small NiO and $NiCr_2O_4$ nanoparticles intimately and uniformly mixed together, charge transfer among the NiO grains was selected as the major conduction channel in this composite, owing to its much lower resistance. And the nanoscale p-p heterojunctions between NiO and $NiCr_2O_4$ nanoparticles played regulatory roles in modulating carrier concentration and thickness of the conduction channels (HAL) near the NiO surfaces.

In order to explain well, schematic diagrams of the gas-sensing mechanism are shown in Fig. 10. On the basis of SEM (Fig. 3d), TEM (Fig. 4h) images and above analyses, the NiO/$NiCr_2O_4$ configuration intimately and uniformly mixed by NiO and $NiCr_2O_4$ nanoparticles is shown in Fig. 10a. And Fig. 10b shows a selected area on the surface of the nanoparticle-aggregated configuration, where a probable conduction channel along low-resistance NiO particles was marked out with red arrows. This kind of conduction was similar to the situation in our previous work [60], where its sensing mechanism was thoroughly discussed, thus a simplified discussion was shown here. Fig. 10c and d respectively show the conduction situations in fresh air and in xylene gas. For the NiO/$NiCr_2O_4$ composite in fresh air, hole accumulation layer (HAL) formed around the surface of p-type NiO, and this HAL shell served as the conduction channel owing to its higher conductivity than that of inner core [5]. Moreover, hole depletion layer (HDL) formed near NiO surface underneath $NiCr_2O_4$ particle, which had a contrary impact on the carrier concentration from HAL, so the resistance of NiO/$NiCr_2O_4$ nanocomposite was higher than that of pure NiO. When the composite was in xylene gas, electrons would be released back from gas-oxidation reaction to p-type semiconductors, breaking the dynamic carrier balance between NiO and $NiCr_2O_4$ particles and increasing the material resistance. Accordingly, with extra

**Table 1**
Comparison of xylene sensing properties among gas sensors based on different sensing materials.

| Materials | T (°C) | Conc. (ppm) | $R_g/R_a$ or $R_a/R_g$ | Detection limit (ppm) | $S_{xylene}/S_{ethanol}$ | Ref. |
|---|---|---|---|---|---|---|
| NiO/$NiMoO_4$ nanocomposite | 400 | 5 | 101.5 | 0.02 | ~5 | [9] |
| 5 at% Cr-doped $Co_3O_4$ | 139 | 5 | 6.4 | 1.15 | ~6 | [47] |
| NiO/$NiWO_4$ composite | 350 | 5 | 343.5 | ~0.02 | 10.5 | [19] |
| Ag@$SnO_2$ core-shell particles | 300 | 5 | 16.2 | — | — | [48] |
| $Cr_2O_3$/$ZnCr_2O_4$ nanocomposite | 275 | 5 | 69.2 | 0.25 | 26.7 | [20] |
| 0.6 at% Pd-doped $WO_3$·$H_2O$ | 230 | 200 | 55.5 | 0.1 | — | [49] |
| 2 at% W-doped NiO | 375 | 200 | 8.7 | ~15 | ~2.8 | [50] |
| 2.04 wt% Au-loaded α-$MoO_3$ | 250 | 100 | 22.1 | 0.5 | ~4.4 | [51] |
| 10 wt% α-$Fe_2O_3$/ $Bi_2WO_6$ | 260 | 100 | 13.5 | — | ~1.9 | [52] |
| 3 at% Sn-doped NiO | 225 | 100 | 20.2 | 0.3 | ~3.4 | [53] |
| 1 at% Y-doped α-$MoO_3$ | 370 | 100 | 28.3 | ~5 | ~3.1 | [10] |
| 0.4 wt% Co-doped ZnO | 320 | 100 | 14.8 | — | ~3.6 | [54] |
| NiO/$NiCr_2O_4$ nanocomposite | 225 | 100 | 66.2 | 0.05 | 11.8 | This work |

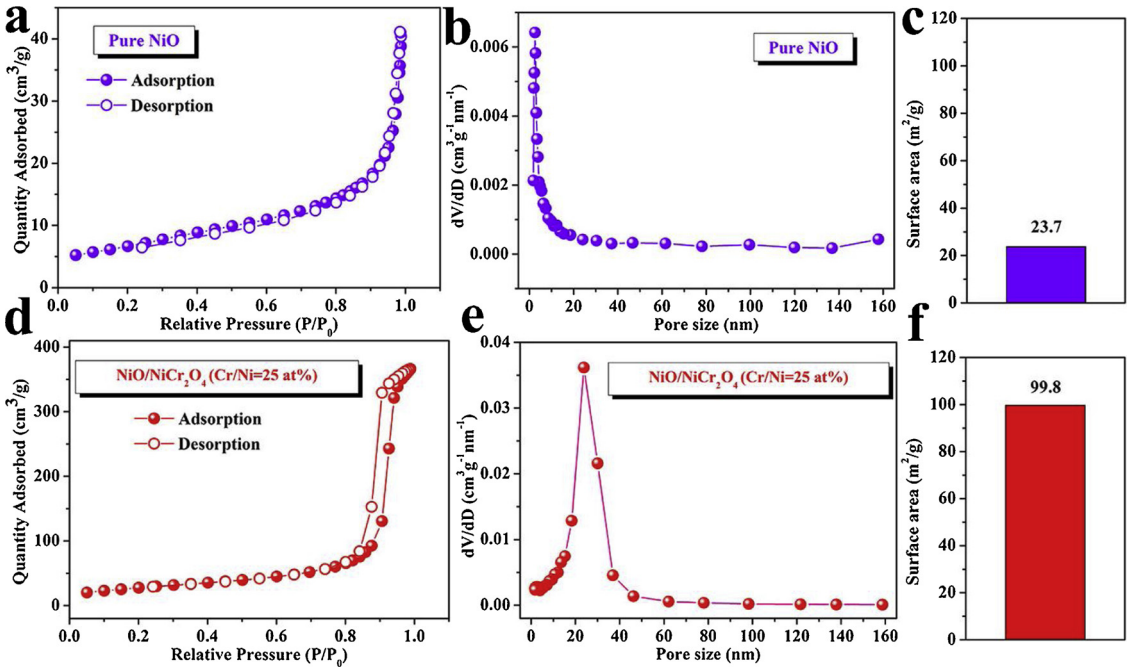


**Fig. 9.** $N_2$ adsorption-desorption isotherms, pore size distributions and BET surface areas of the **(a–c)** NiO and **(d–f)** $NiO/NiCr_2O_4$ (Cr/Ni = 25 at%) samples, respectively.

electrons injected into NiO particles, the hole concentration decreased and the conduction channel (HAL) would get thinner especially in the area underneath the widened hole depletion layer (HDL). In this way, the transfer of conduction carrier was blocked in some way, significantly increasing the sensor resistance [5,23,43]. Namely that the narrowed conduction channel in xylene gas could cause huge enhancement in resistance of the $NiO/NiCr_2O_4$ composite, which was responsible for the ultrasensitive gas detection (high gas response and low detection limit).

The high gas response resulted from the explanations above, however these analyses could not well explain the superior xylene selectivity. NiO is a good catalyst, promoting the adsorption of methyl radicals and oxidizing xylene [9,61]. Meanwhile $NiCr_2O_4$ is also known to be a catalyst for the oxidative dehydrogenation of hydrocarbons such as propane and methane [22,58]. According to the reported researches [9,19,20,25], the gas-sensing reactions can be synergistically promoted through combining two different catalytic sensing materials. Because, the reaction intermediate formed by one catalytic material can further react with or be dissociated by the other adjacent catalytic material in the two-catalyst coexisted sensing material, which can significantly promote the entire gas-sensing reaction. Moreover, it is essential for the maximized promotion to form nanoscale connection among their grains of the catalytic materials, namely the nanoscale sensing material with uniformly mixed configuration by fine catalytic grains is needed for the great synergistic catalytic promotion [9,20]. Note that the higher surface area of small catalytic particles also has beneficial effect on promoting the gas-sensing reaction on the surface. And on the basis of XRD, TEM and BET characterizations before, our obtained $NiO/NiCr_2O_4$ (Cr/Ni = 25 at%) nanocomposite showed the consistent configuration with these benefiting conditions. Accordingly, the high gas response and superior selectivity to xylene of the $NiO/NiCr_2O_4$ nanocomposite was attributed to the synergistic catalytic promotion of the xylene-sensing reaction, owing to the intimate and uniform mixing between the fine NiO and $NiCr_2O_4$ nanoparticles.

## 4. Conclusions

In this paper, $NiO/NiCr_2O_4$ nanocomposites were successfully synthesized and well characterized by XRD, XPS, SEM, TEM and BET techniques. The $NiO/NiCr_2O_4$ (Cr/Ni = 25 at%) sensing material with large surface area and high mesoporosity had a uniformly mixed configuration by many small NiO and $NiCr_2O_4$ nanoparticles, showing not only a high xylene response (66.2–100 ppm) but also a low ppb-level detection limit (1.2–50 ppb). Additionally, this gas sensor exhibited excellent xylene sensitivity with low cross-responses to various interfering gases, giving high response ratios to 100 ppm ethanol ($S_{xylene}/S_{ethanol}$ = 11.8) and acetone ($S_{xylene}/S_{acetone}$ = 10.2) at 225 °C. The ultrasensitive and selective xylene detection of the $NiO/NiCr_2O_4$ gas sensor was attributed to the optimized structural parameters (small grain size, large surface area and high mesoporosity), marked resistive variation due to the formation of nanoscale p-p heterojunctions and the synergistic catalytic promotion of xylene-sensing reaction assisted by

**Table 2**
Textural parameters of the prepared pure and compounded sensing materials.

| Samples | BET surface area ($m^2 g^{-1}$) | Pore Volume ($cm^3 g^{-1}$) | Average pore size (nm) |
|---|---|---|---|
| Pure NiO (Cr/Ni = 0 at%) | 23.7 | 0.06 | 10.5 |
| $NiO/NiCr_2O_4$ (Cr/Ni = 10 at%) | 64.9 | 0.71 | 43.7 |
| $NiO/NiCr_2O_4$ (Cr/Ni = 25 at%) | 99.8 | 0.57 | 22.7 |
| $NiO/NiCr_2O_4$ (Cr/Ni = 50 at%) | 82.2 | 0.50 | 24.1 |
| $NiO/NiCr_2O_4$ (Cr/Ni = 75 at%) | 55.0 | 0.51 | 37.1 |
| $NiO/NiCr_2O_4$ (Cr/Ni = 100 at%) | 49.5 | 0.56 | 45.0 |
| Pure $NiCr_2O_4$ (Cr/Ni = 200 at%) | 6.6 | 0.02 | 10.8 |

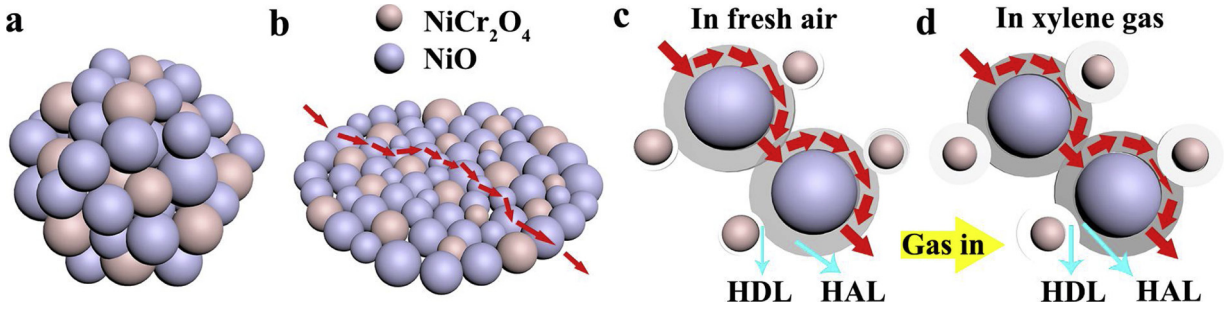


**Fig. 10.** Schematic diagrams of gas sensing mechanism of NiO/$NiCr_2O_4$ p-p nanoparticles.

the uniformly mixed NiO and $NiCr_2O_4$ nanoparticles.

## Acknowledgments

This work is supported by the National Key Research and Development Program (No. 2016YFC0207300). National Natural Science Foundation of China (Nos. 61722305, 61833006, 61520106003). Science and Technology Development Program of Jilin Province (No. 20170520162JH). China Postdoctoral Science Foundation funded projects Nos. 2017T100208 and 2015M580247.

## Appendix A. Supplementary data

Supplementary material related to this article can be found, in the online version, at doi:https://doi.org/10.1016/j.snb.2018.12.152.

## References

[1] M. Hübner, C.E. Simion, A. Tomescu-Stanoiu, S. Pokhrel, N. Bârsan, U. Weimar, Influence of humidity on CO sensing with p-type CuO thick film gas sensors, Sens. Actuators B Chem. 153 (2011) 347–353.
[2] C.P. Gu, X.J. Xu, J.R. Huang, W.Z. Wang, Y.F. Sun, J.H. Liu, Porous flower-like $SnO_2$ nanostructures as sensitive gas sensors for volatile organic compounds detection, Sens. Actuators B Chem. 174 (2012) 31–38.
[3] V.B. Kamble, A.M. Umarji, Gas sensing response analysis of p-type porous chromium oxide thin films, J. Mater. Chem. C Mater. Opt. Electron. Devices 1 (2013) 8167–8176.
[4] R.G. Pavelko, A.A. Vasiliev, E. Llobet, V.G. Sevastyanov, N.T. Kuznetsov, Selectivity problem of $SnO_2$ based materials in the presence of water vapors, Sens. Actuators B Chem. 170 (2012) 51–59.
[5] H.-J. Kim, J.-H. Lee, Highly sensitive and selective gas sensors using p-type oxide semiconductors: overview, Sens. Actuators B Chem. 192 (2014) 607–627.
[6] J.-W. Yoon, J.-K. Choi, J.-H. Lee, Design of a highly sensitive and selective $C_2H_5OH$ sensor using p-type $Co_3O_4$ nanofibers, Sens. Actuators B Chem. 161 (2012) 570–577.
[7] H.-J. Kim, J.-W. Yoon, K.-I. Choi, H.W. Jang, A. Umar, J.-H. Lee, Ultraselective and sensitive detection of xylene and toluene for monitoring indoor air pollution using Cr-doped NiO hierarchical nanostructures, Nanoscale 5 (2013) 7066–7073.
[8] X. Liu, S.T. Cheng, H. Liu, S. Hu, D.Q. Zhang, H.S. Ning, A survey on gas sensing technology, Sensors 12 (2012) 9635–9665.
[9] B.-Y. Kim, J.H. Ahn, J.-W. Yoon, C.-S. Lee, Y.C. Kang, F. Abdel-Hady, A.A. Wazzan, J.-H. Lee, Highly selective xylene sensor based on NiO/$NiMoO_4$ nanocomposite hierarchical spheres for indoor air monitoring, ACS Appl. Mater. Interfaces 8 (2016) 34603–34611.
[10] H.Y. Qin, J. Xie, H. Xu, Y.Z. Li, Y.L. Cao, Green solid-state chemical synthesis and excellent xylene-detecting behaviors of Y-doped α-$MoO_3$ nanoarrays, Mater. Res. Bull. 93 (2017) 256–263.
[11] G. Korotcenkov, B.K. Cho, Engineering approaches for the improvement of conductometric gas sensor parameters Part 1. Improvement of sensor sensitivity and selectivity (short survey), Sens. Actuators B 188 (2013) 709–728.
[12] T.T. Zhou, Y.T. Sang, X.X. Wang, C.Y. Wu, D.W. Zeng, C.S. Xie, Pore size dependent gas-sensing selectivity based on ZnO@ZIF nanorod arrays, Sens. Actuators B Chem. 258 (2018) 1099–1106.
[13] S. Chakraborty, A. Sen, H.S. Maiti, Selective detection of methane and butane by temperature modulation in iron doped tin oxide sensors, Sens. Actuators B Chem. 115 (2006) 610–613.
[14] T. Jinkawa, G. Sakai, J. Tamaki, N. Miura, N. Yamazoe, Relationship between ethanol gas sensitivity and surface catalytic property of tin oxide sensors modified with acidic or basic oxides, J. Mol. Catal. A Chem. 155 (2000) 193–200.
[15] A. Cabot, J. Aribio, A. Cornet, J.R. Morante, F.L. Chen, M.L. Liu, Mesoporous catalytic filters for semiconductor gas sensors, Thin Solid Films 436 (2003) 64–69.
[16] M. Penza, C. Martucci, G. Cassano, $NO_x$ gas sensing characteristics of $WO_3$ thin films activated by noble metals (Pd, Pt, Au) layers, Sens. Actuators B Chem. 50 (1998) 52–59.
[17] M.L. Kantam, P. Sreekanth, K.K. Rao, T.P. Kumar, B.P.C. Rao, B.M. Choudary, An improved process for selective liquid-phase air oxidation of toluene, Catal. Lett. 81 (2002) 223–232.
[18] Y.X. Liu, H.X. Dai, J.G. Deng, S.H. Xie, H.G. Yang, W. Tan, W. Han, Y. Jiang, G.S. Guo, Mesoporous $Co_3O_4$-supported gold nanocatalysts: highly active for the oxidation of carbon monoxide, benzene, toluene, and o-xylene, J. Catal. 309 (2014) 408–418.
[19] T.-H. Kim, C.-H. Kwak, J.-H. Lee, NiO/$NiWO_4$ composite yolk-shell spheres with nanoscale NiO outer layer for ultrasensitive and selective detection of subppm-level p-xylene, ACS Appl. Mater. Interfaces 9 (2017) 32034–32043.
[20] J.-H. Kim, H.-M. Jeong, C.W. Na, J.-W. Yoon, F. Abdel-Hady, A.A. Wazzan, J.-H. Lee, Highly selective and sensitive xylene sensors using $Cr_2O_3$-$ZnCr_2O_4$ heteronanostructures prepared by galvanic replacement, Sens. Actuators B Chem. 235 (2016) 498–506.
[21] C.L. Honeybourne, R.K. Rasheed, Nitrogen dioxide and volatile sulfide sensing properties of copper, zinc and nickel chromite, J. Mater. Chem. 6 (1996) 277–283.
[22] J. Sloczynski, J. Ziolkowski, B. Grzybowska, R. Grabowski, D. Jachewicz, K. Wcislo, L. Gengembre, Oxidative dehydrogenation of propane on $Ni_xMg_{1-x}Al_2O_4$and $NiCr_2O_4$ spinels, J. Catal. 187 (1999) 410–418.
[23] H.-J. Kim, H.-M. Jeong, T.-H. Kim, J.H. Chung, Y.C. Kang, J.-H. Lee, Enhanced ethanol sensing characteristics of $In_2O_3$-decorated NiO hollow nanostructures via modulation of hole accumulation layer, ACS Appl. Mater. Interfaces 6 (2014) 18197–18204.
[24] B.P.J. de Lacy Costello, R.J. Ewen, P.R.H. Jones, N.M. Ratcliffe, R.K.M. Wat, A study of the catalytic and vapour-sensing properties of zinc oxide and tin dioxide in relation to 1-butanol and dimethyldisulphide, Sens. Actuators B Chem. 61 (1999) 199–207.
[25] C.-S. Lee, I.-D. Kim, J.-H. Lee, Selective and sensitive detection of trimethylamine using ZnO-$In_2O_3$ composite nanofibers, Sens. Actuators B Chem. 181 (2013) 463–470.
[26] J. Tang, S.B. Ni, Q.C. Chen, X.L. Yang, L.L. Zhang, Optimized fabrication of $NiCr_2O_4$ and its electrochemical performance in half-cell and full-cell lithium ion batteries, J. Alloys. Compd. 698 (2017) 121–127.
[27] Z.W. Wang, S.K. Saxena, P. Lazor, H.S.C. O'Neill, An in situ Raman spectroscopic study of pressure induced dissociation of spinel $NiCr_2O_4$, J. Phys. Chem. Solids 64 (2003) 425–431.
[28] S.A. Shobeiri, M. Mousavi-Kamazani, F. Beshkar, Facile mechanical milling synthesis of $NiCr_2O_4$ using novel organometallic precursors and investigation of its photocatalytic activity, J. Mater. Sci. Mater. Electron. 28 (2017) 8108–8115.
[29] S.A. Bakar, N. Soltani, W.M.M. Yunus, E. Saion, A. Bahrami, Structural and paramagnetic behavior of spinel $NiCr_2O_4$ nanoparticles synthesized by thermal treatment method: effect of calcination temperature, Solid State Commun. 192 (2014) 15–19.
[30] M. Ptak, M. Maczka, A. Gągor, A. Pikul, L. Macalik, J. Hanuza, X.R.D. Temperature-dependent, IR, magnetic, SEM and TEM studies of Jahn-Teller distorted $NiCr_2O_4$ powders, J. Solid State Chem. 201 (2013) 270–279.
[31] Z.Q. Zhu, X.D. Cheng, W.P. Ye, J. Min, Synthesis of $NiCr_2O_4$ spinel coatings with high emissivity by plasma spraying, Int. J. Min. Met. Mater. 19 (2012) 266–270.
[32] M. Enhessari, A. Salehabadi, S. Khanahmadzadeh, K. Arkat, J. Nouri, Modified sol-gel processing of $NiCr_2O_4$ nanoparticles; structural analysis and optical band gap, High Temp. Mater. Process. 36 (2017) 121–125.
[33] T.D. Sparks, M.C. Kemei, P.T. Barton, R. Seshadri, Magnetocapacitance as a sensitive probe of magnetostructural changes in $NiCr_2O_4$, Phys. Rev. B 89 (2014) 024405.
[34] P. Mohanty, C.J. Sheppard, A.R.E. Prinsloo, W.D. Roos, L. Olivi, G. Aquilanti, Effect of cobalt substitution on the magnetic properties of nickel chromite, J. Magn. Magn. Mater. 451 (2018) 20–28.
[35] J.J. Ma, S.B. Ni, J.C. Zhang, X.L. Yang, L.L. Zhang, The electrochemical performance of nickel chromium oxide as a new anode material for lithium ion batteries, Electrochim. Acta 176 (2015) 1420–1426.
[36] N.-H. Li, Y.-H. Chen, C.-Y. Hu, C.-H. Hsieh, S.-L. Lo, Stabilization of nickel-laden sludge by a high-temperature $NiCr_2O_4$ synthesis process, J. Hazard. Mater. 198 (2011) 356–361.
[37] Y.Z. Guan, C.H. Li, X.Y. Cheng, B. Wang, R.Z. Sun, X.S. Liang, J.H. Zhao, H. Chen, G.Y. Lu, Highly sensitive mixed-potential-type $NO_2$ sensor with YSZ processed using femtosecond laser direct writing technology, Sens. Actuators B Chem. 198 (2014) 110–113.

[38] S. Zhuiykov, T. Nakano, A. Kunimoto, N. Yamazoe, N. Miura, Potentiometric $NO_x$ sensor based on stabilized zirconia and $NiCr_2O_4$ sensing electrode operating at high temperatures, Electrochem. Commun. 3 (2001) 97–101.
[39] H. Zhang, X.Y. Cheng, R.Z. Sun, Y.Z. Guan, Y.W. Liu, C.G. Yin, X.S. Liang, G.Y. Lu, Enhanced chlorine sensing performance of the sensor based NASICON and Cr-series spinel-type oxide electrode with aging treatment, Sens. Actuators B Chem. 198 (2014) 26–32.
[40] M. Stranzenbach, E. Gramckow, B. Saruhan, Planar, impedance-metric $NO_x$-sensor with spinel-type SE for high temperature applications, Sens. Actuators B Chem. 127 (2007) 224–230.
[41] M. Stranzenbach, B. Saruhan, Equivalent circuit analysis on $NO_x$ impedance-metric gas sensors, Sens. Actuators B Chem. 137 (2009) 154–163.
[42] M.J. Dai, L.P. Zhao, H.Y. Gao, P. Sun, F.M. Liu, S.A. Zhang, K. Shimanoe, N. Yamazoe, G.Y. Lu, Hierarchical assembly of $\alpha$-$Fe_2O_3$ nanorods on multiwall carbon nanotubes as a high-performance sensing material for gas sensors, ACS Appl. Mater. Interfaces 9 (2017) 8919–8928.
[43] H.Y. Gao, Q. Yu, K. Chen, P. Sun, F.M. Liu, X. Yan, F.M. Liu, G.Y. Lu, Ultrasensitive gas sensor based on hollow tungsten trioxide-nickel oxide ($WO_3$-NiO) nanoflowers for fast and selective xylene detection, J. Colloid Interface Sci. 535 (2019) 458–468.
[44] O. Lupan, V. Cretu, V. Postica, N. Ababii, O. Polonskyi, V. Kaidas, F. Schutt, Y. Mishra, E. Monaico, I. Tiginyanu, V. Sontea, T. Strunskus, F. Faupel, R. Adelung, Enhanced ethanol vapor sensing performances of copper oxide nanocrystals with mixed phases, Sens. Actuators B Chem. 224 (2016) 434–448.
[45] J.-H. Lee, Gas sensors using hierarchical and hollow oxide nanostructures: overview, Sens. Actuators B Chem. 140 (2009) 319–336.
[46] B. Beverskog, I. Puigdomenech, Pourbaix diagrams for the ternary system of iron-chromium-nickel, Corrosion 55 (1999) 1077–1087.
[47] Y.J. Li, X.H. Ma, S.J. Guo, B. Wang, D.M. Sun, X.D. Zhang, S.P. Ruan, Hydrothermal synthesis and enhanced xylene-sensing properties of pompon-like Cr-doped $Co_3O_4$ hierarchical nanostructures, RSC Adv. 6 (2016) 22889–22895.
[48] P. Rai, S.M. Majhi, Y.-T. Yu, J.-H. Lee, Synthesis of plasmonic Ag@$SnO_2$ core-shell nanoreactors for xylene detection, RSC Adv. 5 (2015) 17653–17659.
[49] F. Li, Q.X. Qin, N. Zhang, C. Chen, L. Sun, X. Liu, Y. Chen, C.N. Li, S.P. Ruan, Improved gas sensing performance with Pd-doped $WO_3{\cdot}H_2O$ nanomaterials for the detection of xylene, Sens. Actuators B Chem. 244 (2017) 837–848.
[50] C.H. Feng, C. Wang, H. Zhang, X. Li, C. Wang, P.F. Cheng, J. Ma, P. Sun, Y. Gao, H. Zhang, Y.F. Sun, J. Zheng, G.Y. Lu, Enhanced sensitive and selective xylene sensors using W-doped NiO nanotubes, Sens. Actuators B Chem. 221 (2015) 1475–1482.
[51] L.L. Sui, X.F. Zhang, X.L. Cheng, P. Wang, Y.M. Xu, S. Gao, H. Zhao, L.H. Huo, Au-loaded hierarchical $MoO_3$ hollow spheres with enhanced gas-sensing performance for the detection of BTX (benzene, toluene, and xylene) and the sensing mechanism, ACS Appl. Mater. Interfaces 9 (2017) 1661–1670.
[52] Z.X. Lin, J.M. Gong, P. Fu, Hierarchical $Fe_2O_3$/$Bi_2WO_6$ nanoplates with enhanced xylene sensing performance, J. Mater. Sci. Mater. Electron. 28 (2017) 4424–4430.
[53] H.Y. Gao, D.D. Wei, P.F. Lin, C. Liu, P. Sun, K. Shimanoe, N. Yamazoe, G.Y. Lu, The design of excellent xylene gas sensor using Sn-doped NiO hierarchical nanostructure, Sens. Actuators B Chem. 253 (2017) 1152–1162.
[54] L. Liu, Z.C. Zhong, Z.J. Wang, L.Y. Wang, S.C. Li, Z. Liu, Y. Han, Y.X. Tian, P.L. Wu, X. Meng, Synthesis, characterization, and m-xylene sensing properties of Co-ZnO composite nanofibers, J. Am. Ceram. Soc. 94 (2011) 3437–3441.
[55] M.E. Franke, T.J. Koplin, U. Simon, Metal and metal oxide nanoparticles in chemiresistors: does the nanoscale matter? Small 2 (2006) 36–50.
[56] N. Barsan, C. Simion, T. Heine, S. Pokhel, U. Weimar, Modeling of sensing and transduction for p-type semiconducting metal oxide based gas sensors, J. Electroceram. 25 (2010) 11–19.
[57] Z.Y. Guo, J.M. Shao, H. Lin, M.D. Jiang, S.Y. Chen, Z.C. Li, Electrical conductivity & temperature sensitivity of ceramics based on NiO simple oxides for NTC applications, J. Mater. Sci. Mater. Electron. 28 (2017) 11871–11877.
[58] W.T. Qi, S.G. Chen, Y.C. Wu, K. Xie, A chromium oxide coated nickel/yttria stabilized zirconia electrode with a heterojunction interface for use in electrochemical methane reforming, RSC Adv. 5 (2015) 47599–47608.
[59] C. Wang, T.S. Wang, B.Q. Wang, X. Zhou, X.Y. Cheng, P. Sun, J. Zheng, G.Y. Lu, Design of $\alpha$-$Fe_2O_3$ nanorods functionalized tubular NiO nanostructure for discriminating toluene molecules, Sci. Rep. 6 (2016) 26432.
[60] H.Y. Gao, L.P. Zhao, L.E. Wang, P. Sun, H.Y. Lu, F.M. Liu, X.H. Chuai, G.Y. Lu, Ultrasensitive and low detection limit of toluene gas sensor based on $SnO_2$-decorated NiO nanostructure, Sens. Actuators B Chem. 255 (2018) 3505–3515.
[61] V. Gaur, A. Sharma, N. Verma, Catalytic oxidation of toluene and m-xylene by activated carbon fiber impregnated with transition metals, Carbon 43 (2005) 3041–3053.